Investigation on corner precision at different corner angles in material extrusion additive manufacturing: An experimental and computational fluid dynamics analysis
(2022) Mollah, Md. Tusher; Moetazedian, Amirpasha; Gleadall, Andy; Yan, Jiongyi; Alphonso, Wayne Edgar; Comminal, Raphaël; Šeta, Berin; Lock, Tony; Spangenberg, Jon

Published in Proceedings for the 2022 International Solid Freeform Fabrication Symposium, University of Texas at Austin.
http://dx.doi.org/10.26153/tsw/44202

Solid Freeform Fabrication 2022: Proceedings of the 33rd Annual International Solid Freeform Fabrication Symposium – An Additive Manufacturing Conference
Reviewed Paper

Investigation on corner precision at different corner angles in material extrusion additive manufacturing: An experimental and computational fluid dynamics analysis

Md. Tusher Mollah*†‖, Amirpasha Moetazedian†, Andy Gleadall†, Jiongyi Yan†, Wayne Edgar Alphonso*, Raphaël Comminal*§, Berin Šeta*, Tony Lock‡, and Jon Spangenberg*

*Department of Civil and Mechanical Engineering, Technical University of Denmark, 2800 Kgs. Lyngby, Denmark.
†Wolfson School of Mechanical and Manufacturing Engineering, Loughborough University, Loughborough, Leicestershire LE11 3TU, United Kingdom.
§Flow Science, Inc., 683 Harkle Road, Santa Fe, NM 87505, USA.
‡Duet3D Ltd, Peterborough PE2 7JE, United Kingdom.
‖Corresponding author: mtumo@mek.dtu.dk

Abstract

This paper investigates the influence of different corner angles on microscale geometry in material extrusion additive manufacturing. Polylactic acid (PLA) was 3D-printed with corner angles of 15°, 30°, 45°, 60°, 75°, 90°, and 135° using Bowden and Direct-drive extruders. A computational fluid dynamics (CFD) model was developed to simulate the polymer flow through the extrusion nozzle of both extruders. The simulated corner geometries were compared with experiments to assess simulation accuracy. This included the primary and secondary mitre cross-sectional width through the corner point of the 3D-printed strands. This enabled a new understanding about the prediction accuracy of the CFD model as well as the state of material at the corners, and the deviation of experimental and simulated corners from the analytical one. Moreover, the amount of over- and under-extrusion around the corner was estimated for experimental and simulated studies compared with the analytical corner, which provided fundamental knowledge on corner precision for angular print paths.

Keywords: Microscale Corner Precision, Bowden and Direct-drive Extruders, Experiments, Computational Fluid Dynamics, Material Extrusion Additive Manufacturing

Introduction

Filament-based Material Extrusion Additive Manufacturing (MEX-AM), also known as Fused Deposition Modelling (FDM) and Fused Filament Fabrication (FFF), is a 3D printing technology where feedstock filament is melted in a liquefier and extruded through a nozzle onto a print platform in layer-wise manner [1–3]. In the last decade, filament-based MEX-AM has evolved from a rapid prototyping tool and is currently used in electronics, medical and automotive sectors [4]. Therefore, a demand for high-quality printed parts with an improved surface roughness [5], high mechanical properties [6], lower internal porosity [3], and high geometrical precision [5] is a growing requirement, in addition to increasing the productivity i.e., reduction in printing time. These properties of the printed part are controlled by the shape of the strands, which typically is a function of two dimensionless parameters- geometrical and speed ratios (i.e., the ratio of layer height by the nozzle diameter and the ratio between printing speed (i.e., speed of nozzle) and extrusion speed (i.e., speed of material extrusion), respectively) [7]. However, it becomes complex when it comes to achieve a precise shape of the strands along the corners, where the print head maneuvers a change in printing direction.

Corner precision in filament-based MEX-AM is affected by common defects such as corner rounding, swelling, and ringing, as reflected in [8]. Corner rounding occurs due to smoothing of the sharp corners where the nozzle executes turns at high speed and can be avoided by implementing lower printing speeds at the cost of increase in printing time [9]. Corner swelling occurs due to over-extrusion of the material at the corner forms wider and thicker strands. Before turning into the corner, the print head must decelerate while the extruder deposits material at a constant rate, leading to a bulge formation. For some systems and materials, this swelling may be reduced by synchronizing the extruder and the printing speed by a closed loop control system with a dynamic calibrated

model of the extruder to manage the time lag. Corner ringing occurs due to vibrations of the printer caused by a sudden change in the printing direction. These defects can be mitigated with lower printing speeds, lower maximum acceleration or by increasing the rigidity of the 3D printer, but such changes may result in improvements for some defects whilst negatively affecting others. Corner defects like the above mentioned were also observed in micro-scale MEX-AM of materials other than thermoplastics, for instance, composite filament printing with acoustophoresis [10]. Solving these issues is non-trivial without a better understanding of the influence of different corner angles and corresponding processing parameters.

Computational Fluid Dynamics (CFD) models predicted the shape and size of the strands printed in MEX-AM under different processing conditions [7,11–14]. The predictions were validated with the experiments in different studies [15–17]. In the case of the filament-based MEX-AM, the material flow through the tiny nozzle is a creeping flow having a very low Reynolds number that can be predicted with a high viscous Newtonian fluid model [18]. Within the same assumption, Comminal et al. [19,20] investigated the sharp and smoothed trajectories of the toolpath of the corner of angles 90° and 30° to analyze the shape of the strand. It was found that the smoothed trajectories result in rounded corners and less over-extrusion; however, the toolpath deviates from its angular shape.

This study focused on the corners between two straight lines with angles of 15°, 30°, 45°, 60°, 75°, 90°, and 135°. The specimens were 3D-printed with PLA using a Bowden extruder and Direct-drive extruder. A CFD model was developed to simulate the corner of different angles for both printing strategies. The shape of the corners in simulations and experiments were compared to analytical geometry expected for the toolpath. The primary and secondary mitre widths were measured in simulations and experiments and compared with the analytical measurements. Moreover, the amount of over- and under-extrusion at the inner- and outer-corners were measured to compare their behavior with the change in angles as well as for both the printing strategies.

Methodology

The MEX-AM experiment was performed using the natural Polylactic acid (PLA) feedstock filament with a diameter of 1.75 mm and density of 1024 $kg.m^{-3}$.The printing parameters and setup can be seen in Figure 1a, where the filament was fed into the nozzle hot-end using a Bowden or Direct-drive extruder. Single-wide-specimens with 10 layers (layer height = 0.2 mm) were printed that comprises seven right trapezoids of investigating corner angles such as 15°, 30°, 45°, 60°, 75°, 90°, and 135°, cf. Figure 1b.

An E3D V6-nozzle of diameter 0.4 mm was used, where the printing speed was set at 2000 $mm.min^{-1}$. The nozzle utilized acceleration and deceleration phases near the corner by the magnitude of 6000 $mm.s^{-2}$. The primary and secondary strands (i.e., before and after turn, respectively) were printed along the x-direction and x, y-directions. Special corner printing parameters such as blending acceleration factor (i.e., the ratio of the acceleration time to the deceleration time) and the jerk speed (i.e., an instantaneous jump of velocity by the amount of jerk when acceleration and deceleration are initiated) were disabled to ensure fundamental understanding to be achieved and for repeatability. The extrusion speed was set to achieve strands width of 0.8 mm. Other widths are the subject of ongoing research. In the case of printing with the Bowden extruder, the extrusion speed was constant throughout the toolpath, whereas the Direct-drive extruder used extrusion speed that was synchronized with the acceleration and deceleration of the nozzle near the corner. The extrusion temperature was set at 210 °C. The experiments were performed in an E3D tool changer because it allowed two different extruders (Bowden or Direct-drive) and a microscope to be implemented in a single hardware system for direct comparability and in-process inspection. Specimens were produced by direct Gcode scripting using open-source software FullControl GCode Designer [21]. After printing the specimens, the microscopic tool was used to capture a series of images of different angles (showed later in this section).

A CFD model was developed in ***FLOW-3D®*** (Version 12.0; 2019; Flow Science, Inc.) [22] in order to mimic the extrusion-deposition flow during printing corners in MEX-AM. The model comprises a cylindrical nozzle mimicking the tip of the E3D V6-nozzle (i.e., a cylinder of 0.4 mm orifice and 1.0 mm outer diameter), and a

static substrate/build plate, as seen in Figure 1c. The cruising speed and acceleration values were imported to model as the experiment was done. However, the extrusion speed was calibrated based on the uniform cross-sectional width of the strands (i.e., 0.8 mm) of the 3D-printed specimens. The simulated length of the strand is 8 mm at either side of the corner. The height of the nozzle end from the substrate was also calibrated to achieve a strand of the height of 0.2 mm, to match printed specimens.

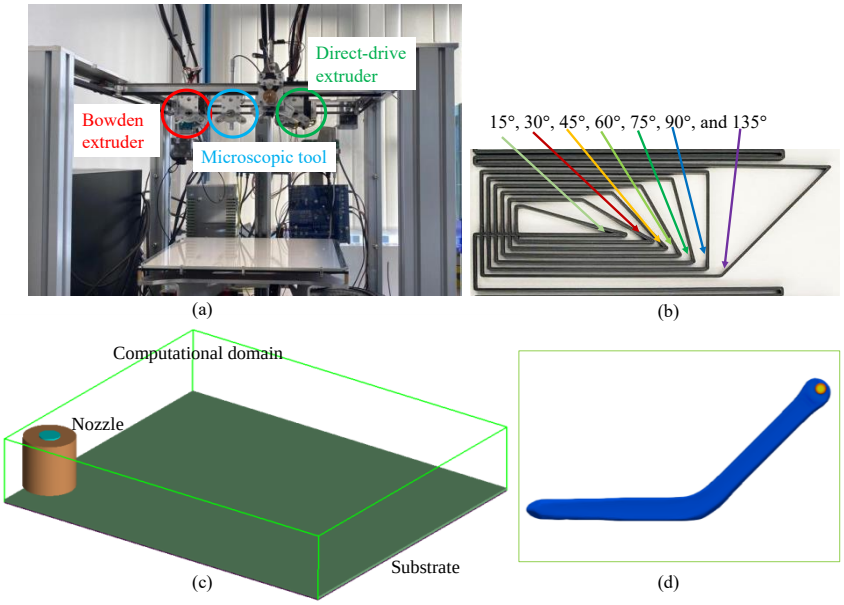

Figure 1: (a) Experimental setup with printing (Bowden and Direct-drive extruders) and microscopic tools; (b) printed sample of different corner angles (for example, Bowden extruder); (c) geometry of the CFD model with nozzle, substrate, and computational domain; and (d) simulated strand of corner angle 135° as an example.

The deposition flow of the material was modeled as a transient and isothermal Newtonian fluid, as in [7,11]. Serdeczny et al. [15] showed that those are sufficient assumption to predict the strands size observed in experiments. Thus, the flow dynamics is governed by the continuity and momentum equations:

$$\nabla . \boldsymbol{q} = 0 \tag{1}$$

$$\rho \left(\frac{\partial \boldsymbol{q}}{\partial t} + \boldsymbol{q} . \nabla \boldsymbol{q} \right) = -\nabla p + \rho \boldsymbol{g_0} + \mu \nabla^2 \boldsymbol{q} \tag{2}$$

where $\boldsymbol{q}$ denotes the velocity vector, p is the pressure, $\boldsymbol{g_0}$ is the acceleration vector due to the gravity $\boldsymbol{g_0} = (0,0,-g_0)$, t is the time, $\rho = 1024$ kg.m^{-3} is the density, and $\mu = 1000$ Pa.s is the constant viscosity of the Newtonian fluid.

The computational domain was meshed with a uniform Cartesian grid and discretized by the Finite Volume Method (FVM). The top plane of the domain was assigned an inlet boundary where an artificial solid object was inserted in order to prevent flow apart from the nozzle orifice. The bottom plane containing the substrate was assigned to a wall boundary condition. Other boundaries were assigned to a continuative boundary condition. The pressure and velocity components are solved implicitly in time. The momentum advection was calculated explicitly with second-order accuracy in space and first-order accuracy in time. Moreover, the free surface was modelled with the Volume of Fluid method (VOF) [23,24].

The microscale geometries of both the printed and simulated strands of all the angles were post-processed using ImageJ® in order to compare the strands shape, measure the primary and secondary mitre cross-sectional widths, and calculate the amount of over- and under-extrusion. The method for post-processing results is presented in Figure 2 for a corner with angle 15° as an example. At first, the experimental microscopy was processed to show the edges of the print, as seen in Figure 2a. This is to compare the experimental prints of Bowden and Direct-drive extruders, as well as to compare those individual ones with the simulated and analytical corners. The

analytical corner (i.e., the horizontal cut in the middle of the oblong shape of the strand) is presented in Figure 2b (left) indicating the double-deposition and analytical underfill phases on the strand. Moreover, the measurements of primary and secondary mitre cross-sectional widths are shown, where the primary one was measured as the distance between the inner-groove and the outer edge through the corner-point at an angle equal to half of the corner, and the secondary one was measured as the distance between the outer edges before and after the turn which is perpendicular to the primary mitre and passes through the corner-point.

Furthermore, all the 3D-printed and simulated strands were compared with the analytical corner in order to calculate the area of over- and under-extrusion observed at the inner- and outer-corners as depicted in Figure 2c. Over-extrusion observed at the inner-corner is defined as inner over-extrusion, whereas under-extrusion was not available. Furthermore, at the outer-edge, over-extrusion observed before and after the turn is defined as outer over-extrusion, whereas under-extrusion observed at the circular track of the corner having a diameter of 0.8 mm (same as the width) is defined as outer under-extrusion. The analytical underfill (Figure 2b) was not occupied by polymer in any specimen, so is not characterized quantitatively.

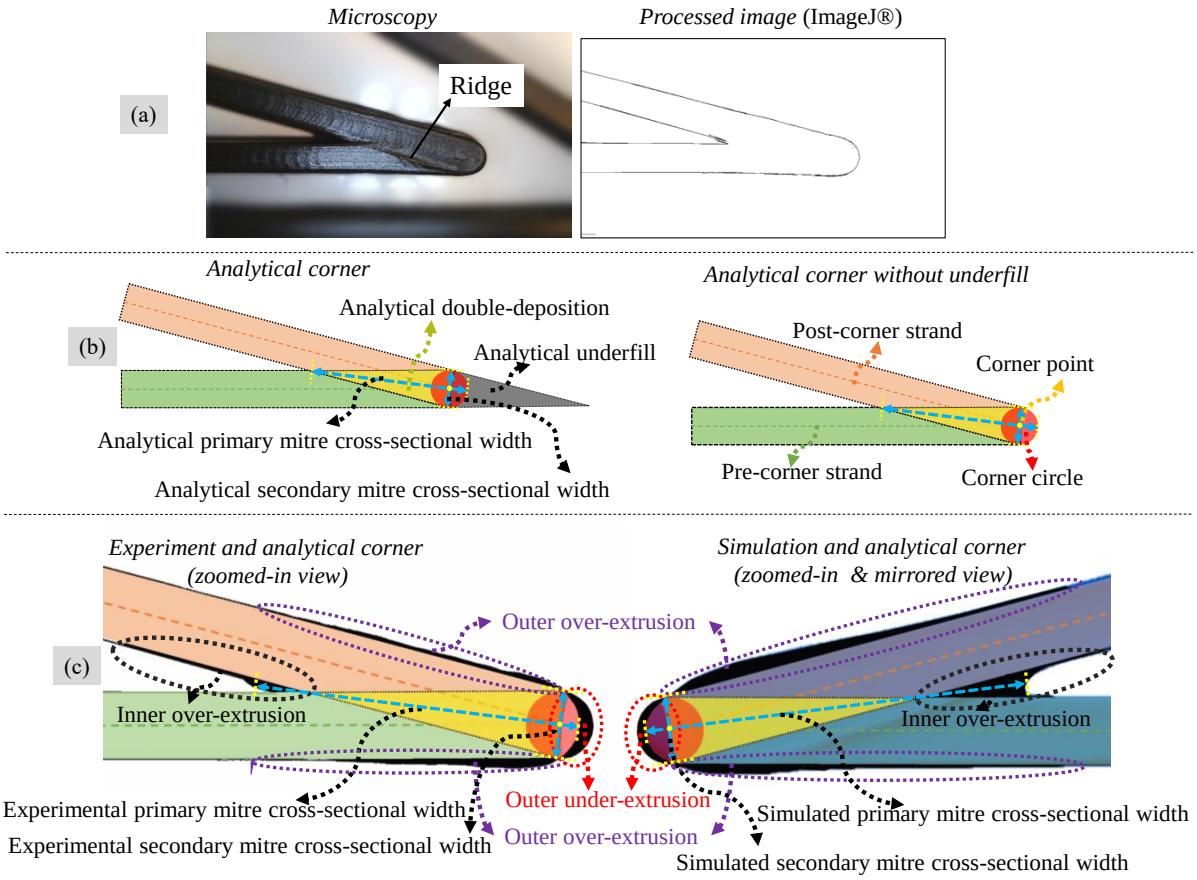

Figure 2: Post-processing of results: (a) processing of microscopy using ImageJ®, (b) Analytical cross-section of corner and measurement of primary and secondary cross-sectional width (left), and Analytical corner without the underfill to compare with experiments and simulations (right), and (c) measurement of over- and under-extrusion of experimental (left) and simulated (right) corners compared to the analytical corner. Moreover, post-processing showed for a corner with angle 15° as an example.

Results and discussion

The MEX-AM experiment and simulated results for different angular turns with angles of 15°, 30°, 45°, 60°, 75°, 90°, and 135° are presented in Figures 3 to 5. Figure 3 shows the microscopic images of the strands obtained using the Bowden extruder as well as simulated strands and a qualitative comparison between the two approaches.

The corner with the largest angle (135°) seemed to have a uniform shape, whereas smaller angles resulted in larger swelling at the corner due to double-deposition. Furthermore, the corner with larger angles appeared to have ringing effect on the surface of the post-corner strand, i.e., the presence of repeated curves on the printed surface. This is typically due to the vibration after the sudden direction change. The ringing seemed to disappear gradually with decreasing the angle. This could be attributed to the amount the double-deposition at the corner, where already deposited material on the pre-corner strands helped in limiting the vibration. Simulations predicted the shape of the corners quite well and were able to predict the existence of a ridge between the pre- and post-corner strands caused by the nozzle ploughing through previously deposited material, as seen in the experiment.

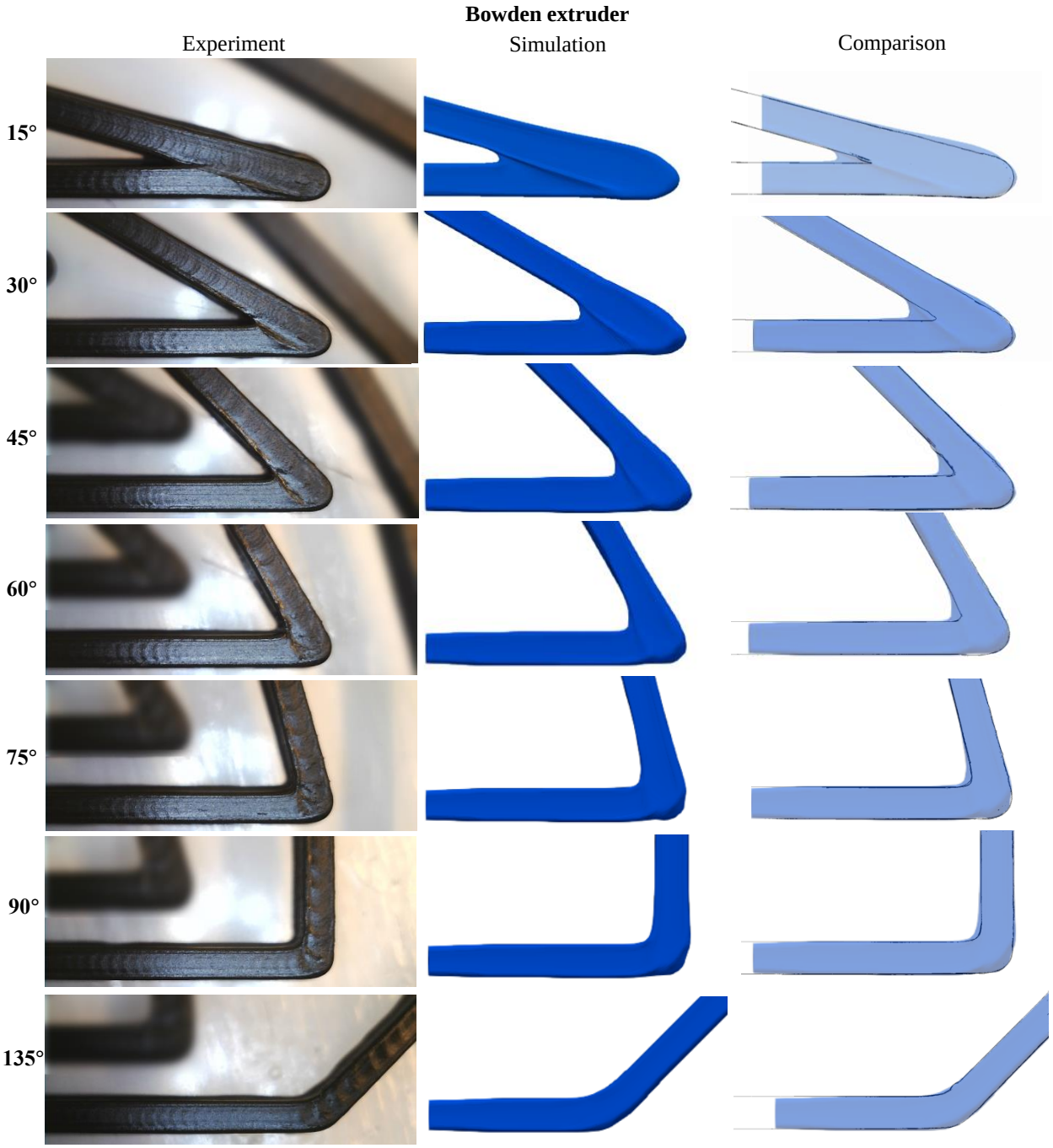

Figure 3: Microscopic images of corners of different angles using Bowden extruder (left column), simulated results (middle column), and comparison between simulations and experiments (right column).

Comparison between experiments and simulations showed that the simulations predict the corners to an acceptable accuracy, cf. Figure 3-right column. However, compared to the experiments, simulations predicted more over-extrusion observed at the inner-corner for most of the angles. This could partly be attributed to the fact that when the nozzle is ploughing through previously deposited material, fluid adjacent to the nozzle moves in the printing direction as well as spreading sideways, therefore, creating wider width. Discrepancies could also come from the Newtonian fluid assumption of the CFD model. Different constitutive fluid models could be tested in future investigations.

Figure 4 presents the microscale images of the corners obtained using the Direct-drive extruder along with the simulated corners and a qualitative comparison between experiment and simulated results. Like the corners from Bowden extruder, the ringing effect observed at the corners with larger angles disappeared gradually when decreasing the angle. Simulations predicted corners quite similar to the ones with Bowden extruder, including the ridge prediction. However, like the Bowden extruder, the observed ridge in the experiments seemed to be larger than the simulations. Furthermore, the ridge in the simulations showed a smooth transition on the presence of material in both phases from pre-corner strand to ridge and from ridge to post-corner strand. On the contrary, a straight transition was observed between the pre-corner strand and ridge in experiment, indicating that the already deposited material in the pre-corner strand may be solidified during printing of the post-corner strand. This effect could be investigated more by including the solidification of strands in the simulations. By qualitative comparison, it appears that the simulations predicted more over-extrusion at the inner-corner than was found experimentally. Moreover, a discrepancy was found in the outer-corner, where the simulations predicted less rounded shape than experiments. This is because the Direct-drive extruder is more responsive than the Bowden one, it may be more able to synchronize extrusion rate with the acceleration and deceleration of the printing speed, and therefore it is expected to have less material extrusion at the corners, which was predicted accurately in the simulations. Although it is dependent on the values of acceleration which determines for how long extrusion is reduced before and after the corner (note that the acceleration is 6000 ms^{-2}). The discrepancy pointed out that the experimental shapes got dominated by additional corner parameters that could be investigated in future studies.

Furthermore, Figure 5(a and b) qualitatively compares the corners at different turns for both Bowden and Direct-drive extruders. The full range of angles can be seen to clearly identify trends in changes to shape and position of the outer edge of the strands. The Direct-drive extruder resulted in more rounded corners than the Bowden extruder, where the outer edge before the turn shifted gradually upwards and left in the figure with the increase in angles. Furthermore, the outer edge after the turn showed a straight release in Bowden extruder, whereas, for Direct-drive extruder, a rounded shape can be seen.

Furthermore, the primary and secondary mitre widths in experiments and simulations, as well as their deviation with the analytical mitre widths, and the amount of over- and under-extrusion were quantified and presented in Figure 5(c to h) for both the Bowden and Direct-drive extruders. It can be seen in Figure 5(c and f) that the primary mitre width for experiments and simulations showed a slight difference for smaller angles, and the difference reduced when the angle was increased for both the extruders. However, an opposite trend was observed in the secondary mitre widths for Bowden and Direct-drive extruders, where Bowden extruder resulted in smaller differences between the experiments and simulations for smaller angles, and the difference increased when increasing the angle. This trend was seen as the Direct-drive simulations extruded less material near the corner point due to the prescribed extrusion speed that was synchronized with the printing speed. In contrast, the experiment was anticipated to be affected by additional corner printing parameters, as discussed in the earlier section. As a result, the secondary mitre width got smaller in simulations and larger in the experiments than the analytical mitre width (i.e., deviation with the negative and positive values, respectively) for Direct-drive extruder, cf. Figure 5g. In contrast, secondary mitre width for Bowden extruder showed minor deviation from the analytical one except for the case of 135°, cf. Figure 5d. Moreover, both the experimental and simulated primary mitre widths observed conspicuous deviation from the analytical one, which reduced as a function of angles as seen in Figure 5(d and g).

Figure 4: Microscopic images of corners of different angles using Direct extruder (left column), simulated results (middle column), and comparison between simulations and experiments (right column).

The area of over- and under-extrusion were measured at both the inner- and outer-sides of the corner for both the experiments (bars with solid border) and simulations (colored bars with dotted border) comparing with the analytical corner. Figure 5(e and h) show the measurement for Bowden and Direct-drive extruders, respectively. It can be seen that the largest area of over-extrusion was observed at the outer corner for the smallest angle in both extruders. Simulations were found to predict more over- and under-extrusion than experiments except for the under-extrusion observed at the outer corner of Bowden extruder, where experiments showed larger under-extrusion. This is simply a consequence of the fact that the corner shape was predicted to be larger in simulations than in experiments, which occupies a greater part of the analytical circle at the corner point. In contrast, over

prediction of the under-extrusion for Direct-drive was observed due to the underfilling of the analytical rectangular pre- and post-corner strands and a part of the circle, which was caused due to the decrease in extrusion speed near the corner point. Furthermore, the over-extrusion at the outer corner in Direct-drive extruder showed a gradual decrease with the angles and met zero over-extrusion for higher angles. Simulated over-extrusion at the inner-corner had a decreasing trend with increasing angles, whereas the experimental one deviates from the trend.

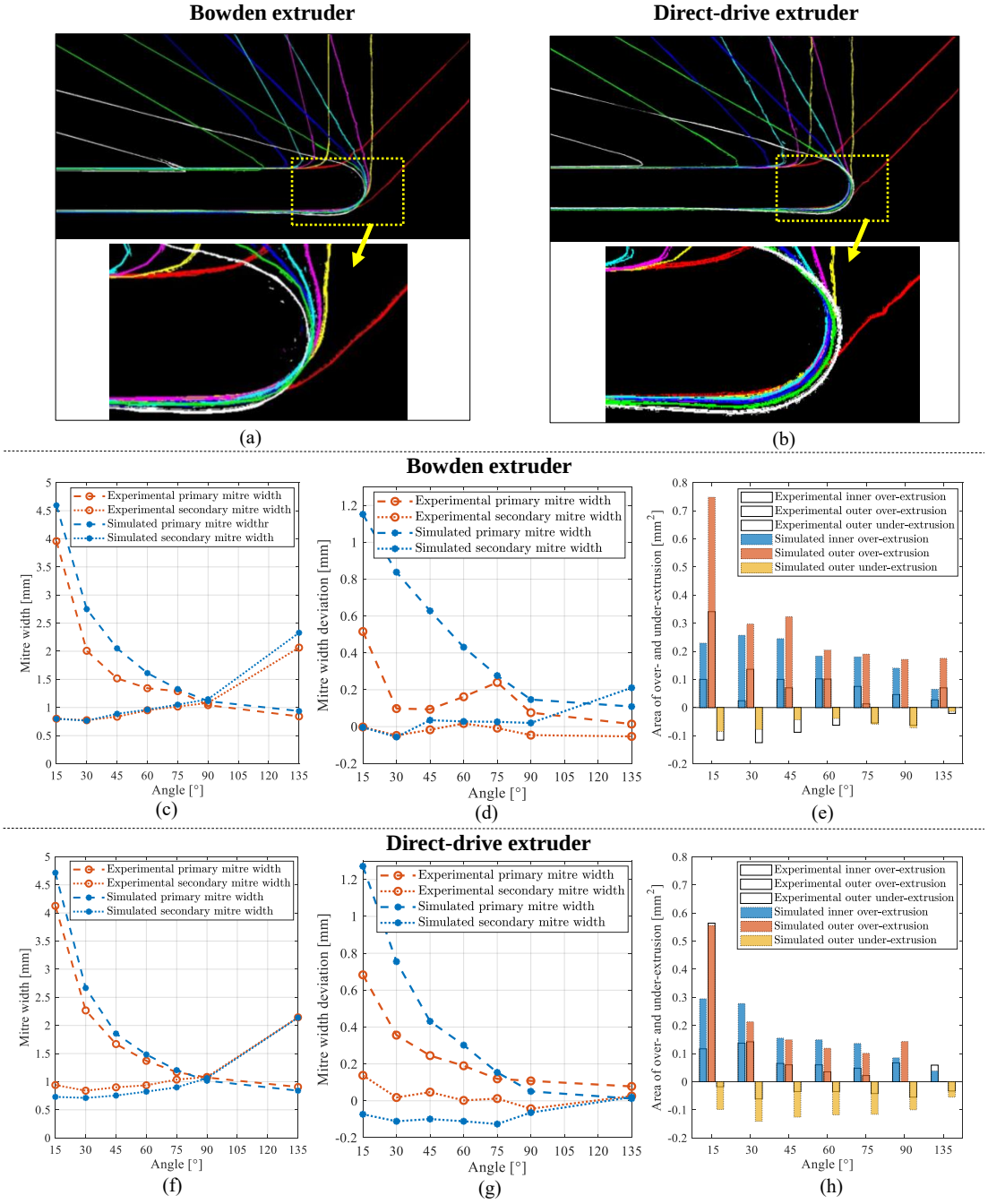

Figure 5: Qualitative and quantitative comparison of corners with different angles: (a) prints with Bowden extruder; (b) prints with Direct extruder; (c) mitre width as a function of angles- Bowden extruder; (d) mitre width deviation as a function of angles- Bowden extruder; (e) over- and under-extrusion as a function of angles- Bowden extruder; (f) mitre width as a function of angles- Direct-drive extruder; (g) mitre width deviation as a function of angles- Direct-drive extruder; (h) over- and under-extrusion as a function of angles- Direct-drive extruder. Moreover, the deviations in Figure 5 (d and g) were calculated relative to the analytical measures.

Conclusion

This study investigated the precision of 3D-printed corners of different angles in filament-based MEX-AM. Two different printing strategies were considered, which include printing with a constant extrusion speed using Bowden extruder and printing with a variable extrusion speed synchronized with the speed of nozzle using Direct-drive extruder. It was found that strands with Direct-drive extruder results in a more rounded shape at the corner of different angles. 3D-printed corners and the simulated corners under the Computational Fluid Dynamics paradigm were compared with the analytical corners. It was seen that the predicted primary and secondary mitre widths in simulations and experiments showed larger deviation with the analytical widths for smaller angles that decreased with increasing angles.

Furthermore, the simulations predict the actual difference between the extruders, where larger under-extrusion was observed at the outer-corner for the Direct-drive due to the syncretized extrusion speed. However, this was not clearly understandable in the experiments indicating the domination of other corner printing parameters. Moreover, the predicted over-extrusion at the inner- and outer-corner in simulations is larger than the one measured in experiment for most of the angles, which is due to the nozzle ploughing within the double-deposition zone. This over prediction could be a drawback of the Newtonian fluid model as there exist an interaction between the fluid strands. The study is currently being extended to investigate several constitutive models as well as the influence of different processing conditions such as nozzle diameter, layer height, acceleration, etc.

Acknowledgements

MTM and JS would like to acknowledge the support from the Danish Council for Independent Research (DFF) | Technology and Production Sciences (FTP) (Contract No. 8022-00042B). Moreover, MTM, WEA, RC, and JS thank ***FLOW-3D***® for their support in regard to licenses. MTM would like to thank Loughborough University for the opportunity to continue an external research stay of four months. Furthermore, he would like to thank Otto Mønsteds Fond and Thomas B. Thriges Fond for their partial funding for the external research stay. AG thanks Sanjay Mortimer from E3D-Online, for supporting the research with an E3D tool changer and for his invaluable advice.

References

[1] B. Brenken, E. Barocio, A. Favaloro, V. Kunc, R.B. Pipes, Fused filament fabrication of fiber-reinforced polymers: A review, Addit. Manuf. 21 (2018) 1–16. https://doi.org/10.1016/j.addma.2018.01.002.

[2] T.D. Ngo, A. Kashani, G. Imbalzano, K.T.Q. Nguyen, D. Hui, Additive manufacturing (3D printing): A review of materials, methods, applications and challenges, Compos. Part B Eng. 143 (2018) 172–196. https://doi.org/10.1016/j.compositesb.2018.02.012.

[3] J. Allum, A. Moetazedian, A. Gleadall, V.V. Silberschmidt, Interlayer bonding has bulk-material strength in extrusion additive manufacturing: New understanding of anisotropy, Addit. Manuf. 34 (2020) 101297. https://doi.org/10.1016/j.addma.2020.101297.

[4] H.K. Dave, J.P. Davim, Materials Forming, Machining and Tribology, in: 2022. http://www.springer.com/series/11181.

[5] M.S. Alsoufi, A.E. Elsayed, How Surface Roughness Performance of Printed Parts Manufactured by Desktop FDM 3D Printer with PLA+ is Influenced by Measuring Direction, Am. J. Mech. Eng. (n.d.) 12.

[6] P. Wang, B. Zou, H. Xiao, S. Ding, C. Huang, Effects of printing parameters of fused deposition modeling on mechanical properties, surface quality, and microstructure of PEEK, J. Mater. Process. Technol. 271 (2019) 62–74. https://doi.org/10.1016/j.jmatprotec.2019.03.016.

[7] R. Comminal, M.P. Serdeczny, D.B. Pedersen, J. Spangenberg, Numerical modeling of the strand deposition flow in extrusion-based additive manufacturing, Addit. Manuf. 20 (2018) 68–76. https://doi.org/10.1016/j.addma.2017.12.013.

[8] D. Halvorson, A Solid Foundation for: High-Quality Corners, Printed Solid, (2016). https://www.printedsolid.com/ blogs/news/a-solid-foundation-for-high-quality-corners. (accessed November 29, 2021).

[9] W. Han, M.A. Jafari, K. Seyed, Process speeding up via deposition planning in fused deposition-based layered manufacturing processes, Rapid Prototyp. J. 9 (2003) 212–218. https://doi.org/10.1108/13552540310489596.
[10] L. Friedrich, M. Begley, Corner accuracy in direct ink writing with support material, Bioprinting. 19 (2020) e00086. https://doi.org/10.1016/j.bprint.2020.e00086.
[11] M.P. Serdeczny, R. Comminal, D.B. Pedersen, J. Spangenberg, Numerical prediction of the porosity of parts fabricated with fused deposition modeling, in: Proc. Annu. Int. Solid Free. Fabr. Symp., Laboratory for Freeform Fabrication, n.d.: pp. 1849–1854.
[12] M.T. Mollah, R. Comminal, M.P. Serdeczny, D.B. Pedersen, J. Spangenberg, Stability and deformations of deposited layers in material extrusion additive manufacturing, Addit. Manuf. (2021) 102193. https://doi.org/10.1016/j.addma.2021.102193.
[13] R. Comminal, M.P. Serdeczny, D.B. Pedersen, J. Spangenberg, Numerical simulation of extrusion-based additive manufacturing – effect of the nozzle geometry on the strand cross-section, in: 18th Int. Conf. Eur. Soc. Precis. Eng. Nanotechnol. Euspen 18, The European Society for Precision Engineering and Nanotechnology, 2018.
[14] M.T. Mollah, R. Comminal, M.P. Serdeczny, D.B. Pedersen, J. Spangenberg, Numerical Predictions of Bottom Layer Stability in Material Extrusion Additive Manufacturing, JOM. (2022). https://doi.org/10.1007/s11837-021-05035-9.
[15] M.P. Serdeczny, R. Comminal, D.B. Pedersen, J. Spangenberg, Experimental validation of a numerical model for the strand shape in material extrusion additive manufacturing, Addit. Manuf. 24 (2018) 145–153. https://doi.org/10.1016/j.addma.2018.09.022.
[16] R. Comminal, W.R. Leal da Silva, T.J. Andersen, H. Stang, J. Spangenberg, Modelling of 3D concrete printing based on computational fluid dynamics, Cem. Concr. Res. 138 (2020) 106256. https://doi.org/10.1016/j.cemconres.2020.106256.
[17] J. Spangenberg, W.R. Leal da Silva, R. Comminal, M.T. Mollah, T.J. Andersen, H. Stang, Numerical simulation of multi-layer 3D concrete printing, RILEM Tech. Lett. 6 (2021) 119–123. https://doi.org/10.21809/rilemtechlett.2021.142.
[18] M.P. Serdeczny, R. Comminal, D.B. Pedersen, J. Spangenberg, Numerical simulations of the mesostructure formation in material extrusion additive manufacturing, Addit. Manuf. 28 (2019) 419–429. https://doi.org/10.1016/j.addma.2019.05.024.
[19] R. Comminal, M.P. Serdeczny, D.B. Pedersen, J. Spangenberg, Numerical Modeling of the Material Deposition and Contouring Precision in Fused Deposition Modeling, in: Proc. Annu. Int. Solid Free. Fabr. Symp., 2018: pp. 1855–1864.
[20] R. Comminal, M.P. Serdeczny, D.B. Pedersen, J. Spangenberg, Motion planning and numerical simulation of material deposition at corners in extrusion additive manufacturing, Addit. Manuf. 29 (2019) 100753. https://doi.org/10.1016/j.addma.2019.06.005.
[21] A. Gleadall, FullControl GCode Designer: Open-source software for unconstrained design in additive manufacturing, Addit. Manuf. 46 (2021) 102109. https://doi.org/10.1016/j.addma.2021.102109.
[22] FLOW-3D® Version 12.0 [Computer software], Santa Fe, NM: Flow Science, Inc., 2019. https://www.flow3d.com (accessed May 10, 2022).
[23] C.W. Hirt, B.D. Nichols, Volume of fluid (VOF) method for the dynamics of free boundaries, J. Comput. Phys. 39 (1981) 201–225. https://doi.org/10.1016/0021-9991(81)90145-5.
[24] R. Comminal, J. Spangenberg, J.H. Hattel, Cellwise conservative unsplit advection for the volume of fluid method, J. Comput. Phys. 283 (2015) 582–608. https://doi.org/10.1016/j.jcp.2014.12.003.